Robust and secure UAV navigation using GNSS, phased-array radio system and inertial sensor fusion

Sigurd M. Albrektsen* Torleiv H. Bryne* Tor A. Johansen†
Department of Engineering Cybernetics
Norwegian University of Science and Technology
Email: *{sigurd.albrektsen, torleiv.h.bryne}@ieee.org †tor.arne.johansen@ntnu.no

***Abstract*— Positioning using global navigation satellite systems (GNSS) has for several years been the de facto method for long-range navigation of ground, marine and aerial vehicles. With global coverage, high accuracy, and lightweight receivers, GNSS positioning has several desirable properties, especially on unmanned aerial systems (UAVs) with limited sensor payload capacity. However, due to the low signal-to-noise ratio (SNR) of the GNSS signals the navigation signal is prone to malicious attacks, such as jamming or spoofing.**

In the last few years, alternative solutions for absolute positioning of unmanned vehicles have emerged. One example of this is positioning using a phased array radio systems (PARS). PARS equipment has the potential to provide position measurements that are accurate within tens of meters. The PARS solutions typically have significantly higher SNR and strongly encrypted messages, which makes them robust towards malicious attacks.

This paper presents a method for an inertial navigation system which is aided using redundant position sensors. The high-accuracy RTK solution is the primary position reference, when it is available. The PARS is used to detect if GNSS solution is being spoofed (or jammed), and is used as the fall-back positioning solution.

I. INTRODUCTION

The most common solution for drift-free positioning has for several years been using global navigation satellite systems (GNSS). This solution has several attractive features: global coverage, lightweight receivers, and high accuracy - especially when using a real-time kinematic (RTK) solution. However, due to the low signal-to-noise ratio (SNR) of GNSS systems, these navigation solutions are prone to jamming [1] and spoofing [2], where the latter got much public attention in January 2016, when a US Navy patrol boat ended up in Iranian territorial waters [3]. In addition, a single error in either hardware or software can inhibit a GNSS positioning solution to work as intended. With more frequent UAV-usage in both the civil and military sector, being able to handle loss of GNSS positioning due to either errors or malicious sources becomes increasingly important.

This work was partly supported by the Norwegian Research Council and through the *Hybrid Operations in Maritime Environments* program at MAROFF together with the FRINATEK projects *Low-Cost Integrated Navigation Systems Using Nonlinear Observer Theory* and *Multi-stage global sensor fusion for navigation using nonlinear observers and eXogenous Kalman filter*, and the Center of *Autonomous Marine Operations and Systems* (AMOS AMOS) at the Norwegian University of Science and Technology (NTNU) (grants no. 269480, 221666, 250725 and 223254).

A study of countermeasures to GNSS spoofing attacks is given in [4], where alterations to existing methods reduce the vulnerability towards spoofing interference by monitoring the GNSS signal over time. These methods do, however, not protect against jamming attacks and hardware failure. As a result they are not sufficient as a redundant navigation system.

In the last few years navigation solutions that uses phased-array radio systems (PARS) have been demonstrated on small UAVs [5]. PARS's primary usage is as a high bandwith radio communication tool, but as it uses electronic beamforming, it also provides measurements which can be used to deduce positioning [6]. This system complements the security aspect of GNSS solutions well, by having a much higher SNR, strongly encrypted communication, being self-contained and being based on a different measurement principle. It does, however, typically have lower accuracy than GNSS solutions.

The proposed strategy for spoofing detection in this paperer is inherently dependent of the accuracy of PARS. Since the positioning is based on both range and direction of arrival of the signal, signal reflections will be an issue. Alternative strategies than the one proposed in this paper can be based on GNSS equipment and advanced integrity monitoring techniques. In [7], the usage of two GNSS receivers for GNSS direction-of-arrival sensing combined with signal distortion detection is advised. The benefit of PARS in this respect, especially compared to civilian GNSS, is that in addition to having encrypted communication, PARS is based on signal direction-of-arrival detection, such than any spoofing attempts has to be carried out in the same sector that is covered by the PARS base antenna.

A. Main Contribution

The main contribution in this paper is the presentation of an inertial navigation system (INS) that uses the highly accurate RTK GNSS positioning solution when it is available, but also detects GNSS spoofing, based on the more secure, but less accurate, PARS positioning system. If GNSS spoofing is detected, PARS will be used as the aiding position sensor.

The solution consists of two observers running in parallel: the first observer using the RTK GNSS solution as the position reference, and the second observer using PARS and barometer measurements as the position reference. The estimates from these observers are inputs to a supervisor

module that detects spoofing, and provides the best available solution.

To verify the solution experimental data from a fixed wing, beyond visual line of sight experiment was used, with a simulated GNSS-spoofing attack added during post-processing.

B. Outline

In this paper we start by defining the preliminaries in Section II, before we introduce the GNSS RTK positioning system and necessary steps needed to use the PARS as a positioning sensor in Section III. We continue with presenting our nonlinear observer for aided INS and spoofing supervisor in Section IV. An experiment was carried out, and a description of the system and hardware used is given in Section V. The results from the experiment are presented in Section VI and conclusive remarks are given in Section VII, along with suggestions for future work.

II. PRELIMINARIES

Before presenting PARS-based positioning, and the PARS-aided INS, we state some preliminaries.

A. Notation

The Euclidean vector norm is denoted $\|\cdot\|_2$. The $n \times n$ identity matrix is denoted $\boldsymbol{I}_n$. Moreover, the transpose of a vector or a matrix is denoted $(\cdot)^\intercal$. Coordinate frames are denoted with $\{\cdot\}$. $\boldsymbol{S}(\cdot) \in SS(3)$ represents the skew symmetric matrix such that $\boldsymbol{S}(z_1)z_2 = z_1 \times z_2$ for two vectors $z_1, z_2 \in \mathbb{R}^3$. In addition, $z^a_{bc} \in \mathbb{R}^3$ denotes a vector z, to frame $\{c\}$, relative $\{b\}$, decomposed in $\{a\}$. Moreover, $\otimes$ denotes the Hamiltonian quaternion product. The diag$(\star, ..., \star)$ function places the n arguments on the diagonal of a square matrix with n rows and n columns.

The rotation matrix, $\boldsymbol{R}^b_a \in SO(3)$, describes the rotation between two given frames $\{a\}$ and $\{b\}$. Equivalently, the rotation between $\{a\}$ and $\{b\}$ may be represented using the unit quaternion $\boldsymbol{q}^b_a = (s, \boldsymbol{r}^\intercal)^\intercal$ where $s \in \mathbb{R}^1$ is the real part of the quaternion and $\boldsymbol{r} \in \mathbb{R}^3$ is the vector part. In addition, the Euler angles (roll, pitch and yaw) are given as

$$\boldsymbol{\Theta} = \begin{pmatrix} \phi, & \theta, & \psi \end{pmatrix}^\intercal. \tag{1}$$

Latitude and longitude on Earth is represented by $\mu \in [-\pi/2, \pi/2]$ and $\lambda \in (-\pi, \pi]$, respectively.

B. Coordinate Frames

This paper considers five coordinate frames. The first four are the Earth Centered Inertial (ECI) frame, the Earth Centered Earth Fixed (ECEF) frame, a tangent frame equivalent of an Earth-fixed North East Down (NED) frame and the BODY reference frame, denoted $\{i\}$, $\{e\}$, $\{t\}$ and $\{b\}$, respectively. The NED directions are respectively denoted N, E, D. See Fig. 1) for details. The fifth coordinate system is called the PARS coordinate systems and is denoted ~~$\{p\}$~~$\{r\}$. The PARS coordinate system resembles the tangent frame, however, horizontally translated and rotated about the tangent frames z-axis, as indicate in Fig. 2.

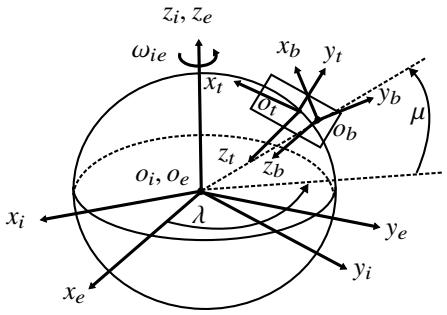

Fig. 1. Definitions of the BODY, Tangent, ECEF and ECI reference frames.

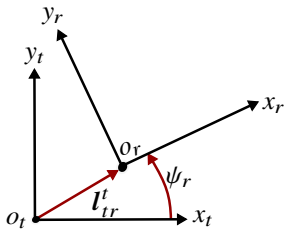

Fig. 2. Relationship between the $\{t\}$ and the $\{r\}$ frame. $\boldsymbol{l}^t_{tr}$ represents the vector from the $\{t\}$ frame to the $\{r\}$ frame. ψ_r represent the azimuth rotation of $\{r\}$ about the $\{t\}$ frame.

C. Inertial Measurement Units

A simplified measurement model of an IMU, providing specific force and angular rate sensor (ARS) measurements, is given as

$$\boldsymbol{f}^b_{\text{IMU}} = \boldsymbol{f}^b_{ib} + \boldsymbol{b}^b_{\text{acc}} + \boldsymbol{w}^b_{\text{acc}}, \tag{2}$$
$$\boldsymbol{\omega}^b_{\text{IMU}} = \boldsymbol{\omega}^b_{ib} + \boldsymbol{b}^b_{\text{ars}} + \boldsymbol{w}^b_{\text{ars}}, \tag{3}$$

where $\boldsymbol{f}^b_{ib}$ is the specific force, relating to the acceleration and gravity vector, $\boldsymbol{g}^t_b = (0, 0, g)^\intercal$ through

$$\begin{aligned} \boldsymbol{f}^b_{ib} &= \boldsymbol{R}^b_n \dot{\boldsymbol{v}}^t_{ib} - \boldsymbol{R}^b_t \boldsymbol{g}^t_b \\ &= \boldsymbol{a}^b_{ib} + \boldsymbol{S}(\boldsymbol{\omega}^b_{ib})\boldsymbol{v}^b_{ib} - \boldsymbol{R}^b_t \boldsymbol{g}^t_b. \end{aligned} \tag{4}$$

$\boldsymbol{\omega}^b_{ib}$ represents angular velocity, while $\boldsymbol{v}^b_{ib}$, represents the BODY-fixed linear velocity. The BODY-fixed acceleration is represented by $\boldsymbol{a}^b_{ib}$, while $\boldsymbol{S}(\boldsymbol{\omega}^b_{ib})\boldsymbol{v}^b_{ib}$ constitutes the centripetal accelerations. $\boldsymbol{b}^b_\star$ represent the accelerometer (ACC) ~~biases~~, and the ARS biases. $\boldsymbol{w}^b_\star$ represent sensor noise.

D. Strapdown Equations

The NLO-based INS is derived using

$$\dot{\boldsymbol{p}}^t_{tb} = \boldsymbol{v}^t_{tb} \tag{5}$$
$$\dot{\boldsymbol{v}}^t_{tb} = -2\boldsymbol{S}(\boldsymbol{\omega}^t_{it})\boldsymbol{v}^t_{tb} + \boldsymbol{R}^t_b \boldsymbol{f}^b_{ib} + \boldsymbol{g}^t_b \tag{6}$$
$$\dot{\boldsymbol{q}}^t_b = \frac{1}{2}\boldsymbol{q}^t_b \otimes \begin{pmatrix} 0 \\ \boldsymbol{\omega}^b_{ib} \end{pmatrix} - \frac{1}{2}\boldsymbol{q}^t_b \otimes \begin{pmatrix} 0 \\ \boldsymbol{\omega}^t_{it} \end{pmatrix} \tag{7}$$

as strapdown equations. Moreover,

$$\boldsymbol{\omega}^t_{it} = \boldsymbol{\omega}^t_{ie} = \begin{pmatrix} \cos(\mu) & 0 & -\sin(\lambda) \end{pmatrix}^\intercal \omega_{ie}, \tag{8}$$

[8], due to $\{t\}$ being Earth fixed and thus $\boldsymbol{\omega}^t_{et} = \boldsymbol{0}_{3\times 1}$. $\boldsymbol{p}^t_{tb}$ and $\boldsymbol{v}^t_{tb}$ represents the position and velocity vectors, respectively.

III. POSITIONING

A. Real-time kinematic GNSS

To improve the accuracy of GNSS positioning systems, the real-time kinematic (RTK) solution is commonly used. By having a stationary ground station with a known location, and comparing the phase of the signal's carrier wave received at the ground station to the measurements received on-board the UAV, the RTK position can be calculated. By multiplying the carrier wavelength with the number of whole cycles between the satellite and the UAV, the phase difference can be compensated for and centimetre-level precision can be achieved.

Due to the high accuracy of the RTK solution, it is desirable to use this as the primary positioning sensor when it is available.

B. Phased Array Radio System Positioning

Although the primary functionality of the PARS is data transfer, the system can also be used as an absolute positioning measurement system. By observing the phase difference of the incoming signal between the different antenna elements in the radio array, the bearing and elevation of the UAV can be observed, in the ground radio's frame of reference, $\{r\}$. There exits a variety of methods that aim to solve this problem of direction-of-arrival (DOA) [9], perhaps most notably Schmidt's MUSIC [10] and Roy and Kaliath's ESPRIT [11]. Furthermore, by accurately timing the transmission time of the signal and subtracting internal processing time, the range measurement is found. To be able to use these measurements for navigation, they need to be rotated and translated into the UAV's positional reference frame. Calculations of the pose from the mobile PARS ground station to the tangent frame is described in [5]. As the calculation of the PARS measurements are done on the ground, a minimal amount of processing power is needed by the computer on-board the UAV.

The PARS range, elevation and bearing measurements can be used to calculate the relative position of the UAV in a local Earth-fixed frame. When using the tangent frame, as done in this paper, the range/bearing measurements related to the UAV position, through the radio coordinate system $\{r\}$ using,

$$\rho_m = \rho_u + \varepsilon_\rho, \tag{9}$$

$$\psi_m = \psi_u + \varepsilon_\psi, \tag{10}$$

$$\theta_m = \theta_u + \varepsilon_\theta, \tag{11}$$

where

$$\rho_u = \|\boldsymbol{p}^r_{\text{PARS}}\|_2, \tag{12}$$

$$\tan(\psi_u) = p^r_{rb,y}/p^r_{rb,x}, \tag{13}$$

$$\tan(\theta_u) = -p^r_{rb,z}/\rho_{\text{hor}} \tag{14}$$

with $\|\boldsymbol{p}^r_{\text{PARS}}\|_2 = \sqrt{(p^r_{rb,x})^2 + (p^r_{rb,y})^2 + (p^r_{rb,z})^2}$ and $\bar{\rho}_u = \sqrt{(p^r_{rb,x})^2 + (p^r_{rb,y})^2}$, while $\varepsilon_\star$ represents noise. Moreover, the relationships of (12)–(14) are similar to those in [12, Ch. 13.6.2.2], used for radar tracking of aircraft, and can derived from

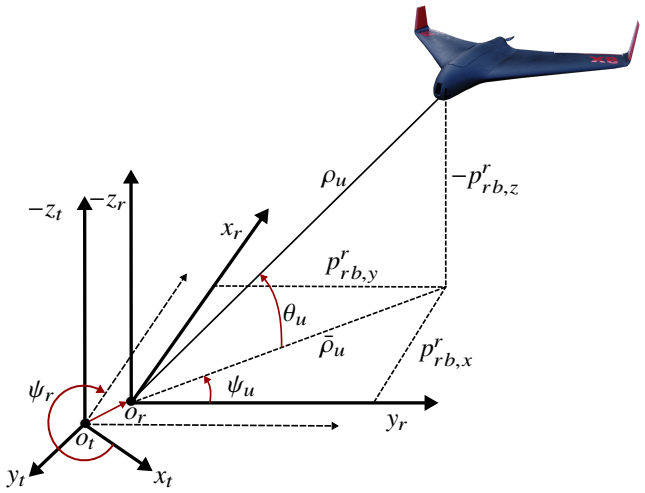

Fig. 3. Range/bearing measurements. The red vector denotes the vector from the $\{t\}$ frame to the $\{r\}$, given in the $\{t\}$ frame, denoted $\boldsymbol{l}^r_{tr}$. The angle ψ_r represents the azimuth angle between the $\{t\}$ frame and the $\{t\}$ frame.

$$\boldsymbol{p}^r_{\text{PARS}} = \begin{pmatrix} p^r_{rb,x} \\ p^r_{rb,y} \\ p^r_{rb,z} \end{pmatrix} = \begin{pmatrix} \rho_u \cos(\psi_u)\cos(\theta_u) \\ \rho_u \sin(\psi_u)\cos(\theta_u) \\ -\rho_u \sin(\theta_u)) \end{pmatrix}. \tag{15}$$

according to Fig. 3. Based on (15), the PARS position is given in the tangent frame as $\boldsymbol{p}^t_{\text{PARS}} = \boldsymbol{R}^t_r(\psi_r)\boldsymbol{p}^r_{\text{PARS}} + \boldsymbol{l}^t_{tr}$, where $\boldsymbol{l}^t_{tr}$ is the vector from the $\{t\}$ frame to the $\{r\}$ frame, decomposed in the $\{t\}$. ψ_r represents the azimuth angle from $\{t\}$ to $\{r\}$. ψ_r is obtained in during calibration of the PARS ground antenna.

C. PARS and barometer positioning

The results presented in [5] show that the vertical PARS position measurement based on the range and elevation angle is some times very noisy, likely due to reflections in the ocean surface.

Therefore, the vertical measurement in (15) was replaced with an altitude measurement based on barometric pressure $\gamma_{\text{BARO},m} = p^r_{\text{BARO},z} + \varepsilon_{\text{BARO}}$. Moreover, to prevent the elevation angle measurement to affect the horizontal positioning, the PARS range was altitude compensated using the barometer measurement

$$\bar{\rho}_m = \sqrt{\rho_m^2 - \gamma^2_{\text{BARO},m}}, \tag{16}$$

where $\bar{\rho}_m$ then becomes a measurement of horizontal range $\bar{\rho}_u = \sqrt{(p^r_{rb,x})^2 + (p^r_{rb,y})^2}$, cf. Fig. 3, such that Cartesian position measurement becomes,

$$\boldsymbol{p}^r_{\text{PARS,BARO}} = \begin{pmatrix} \bar{\rho}_m \cos(\psi_m) \\ \bar{\rho}_m \sin(\psi_m) \\ \gamma_{\text{BARO},m} \end{pmatrix}, \tag{17}$$

decoupling the horizontal components of the measurement $\boldsymbol{p}^r_{\text{PARS,BARO}}$ from the elevation angle measurement. Furthermore, the covariance of $\boldsymbol{p}^r_{\text{PARS,BARO}}$, denoted $\bar{\boldsymbol{R}}(t)$, is based

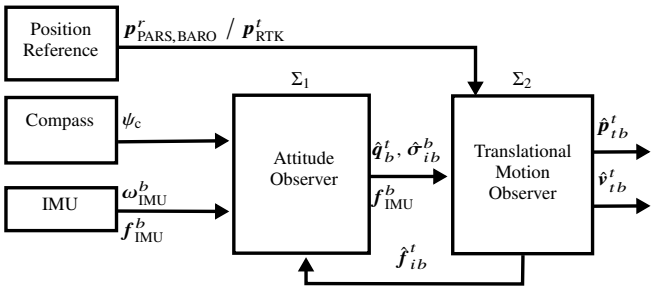

Fig. 4. Feedback-interconnected observer framework. The observer design is based upon integration of ARS and ACC measurements. The compass measurement ψ_c is used as a aiding heading measurements in the nonlinear observer. In addition, the two position references $\boldsymbol{p}^r_{\text{PARS,BARO}}$ or $\boldsymbol{p}^t_{\text{RTK}}$, given in the $\{r\}$ and $\{t\}$ frames, are used to aid the translational motion observer.

on the original measurements, ρ_m, ψ_m and $\gamma_{\text{BARO},m}$ and their covariance $\boldsymbol{R}_{\text{PARS}}(t) = \text{diag}\left(E[\varepsilon_\rho^2], E[\varepsilon_\psi^2], E[\varepsilon_{\text{BARO}}^2]\right)$. $\bar{\boldsymbol{R}}(t) = \boldsymbol{M}(t)\boldsymbol{R}_{\text{PARS}}(t)\boldsymbol{M}^\intercal(t)$ is derived through linearization [13, Ch. 1.6] by assuming that the noise is Gaussian, where $\boldsymbol{M}(t)$ is the Jacobian of $p^r_{\text{PARS,BARO}}$ w.r.t. to the noise $\boldsymbol{\varepsilon} = \begin{pmatrix}\varepsilon_\rho & \varepsilon_\psi & \varepsilon_{\text{BARO}}\end{pmatrix}^\intercal$. This results in:

$$\boldsymbol{M}(t) = \frac{\partial \boldsymbol{p}^r_{\text{PARS,BARO}}}{\partial \boldsymbol{\varepsilon}} = \begin{pmatrix} m_{11} & m_{12} & m_{13} \\ m_{21} & m_{22} & m_{23} \\ 0 & 0 & 1 \end{pmatrix} \tag{18}$$

with

$$\begin{aligned} m_{11} &= \frac{\cos(\psi_m)\rho_m}{\bar{\rho}_m} & m_{21} &= \frac{\sin(\psi_m)\rho_m}{\bar{\rho}_m} \\ m_{12} &= -\sin(\psi_m)\bar{\rho}_m & m_{22} &= \cos(\psi_m)\bar{\rho}_m \\ m_{13} &= -\frac{\cos(\psi_m)\gamma_{\text{BARO},m}}{\bar{\rho}_m} & m_{23} &= -\frac{\sin(\psi_m)\gamma_{\text{BARO},m}}{\bar{\rho}_m}. \end{aligned}$$

In addition, the measurement (17) can be given directly in the $\{t\}$ frame by taking $\boldsymbol{p}^t_{\text{PARS,BARO}} = \boldsymbol{R}^t_r \boldsymbol{p}^r_{\text{PARS,BARO}}$ and transforming the corresponding covariance to the $\{t\}$ frame using

$$\bar{\boldsymbol{R}}(t) = \boldsymbol{R}^t_r \boldsymbol{M}(t)\boldsymbol{R}_{\text{PARS}}(t)\boldsymbol{M}^\intercal(t)\boldsymbol{R}^r_t. \tag{19}$$

IV. SYSTEM IMPLEMENTATION

A. NLO and TMO observers

The observer design consist of two feedback-interconnected observers, similar to [6], as depicted in Fig. 4 and based upon the strapdown equations (5)–(7). The first observer is a nonlinear attitude observer, estimating attitude and the ~~gyro~~ARS bias. The second observer is a translational motion observer estimating position, velocity and specific force given in the navigation frame. These observers are referred to as the NLO and TMO respectively in this paper. The observer framework is structurally the same as in [14], where the attitude between the $\{b\}$ and the $\{e\}$ frame was estimated.

The error dynamics of the feedback interconnected observer is uniformly semiglobal exponentially stable, under certain conditions, with positive definite matrices $\boldsymbol{Q}$ and $\bar{\boldsymbol{R}}$, see [14] for details.

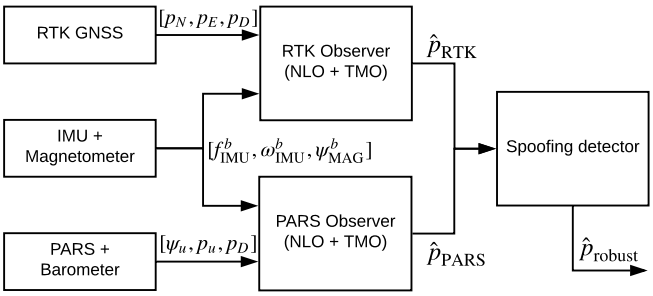

Fig. 5. Spoofing prevention system overview.

To account for any colored noise in the PARS measurements, additional states can be introduced such as in [15]. By choosing appropriated error states and corresponding models, the gain of the TMO can use a time-scaled Riccati equation that can account for the additional uncertainty when propagating the covariance[16].

B. Spoofing detector

An overview of the spoofing prevention system is given in Fig. 5. The concept of the spoofing detector is the base assumption that the PARS as a positioning system cannot easily be spoofed due to:

- The high signal-to-noise ratio
- Only signals originated inside of the visible sector of the radio are considered in the DOA calcualtion
- The communication on the PARS-network is encrypted, ensuring the sender's origin

There are, however, a different set of challenges with the PARS, such as reflections and inaccuracies in the algorithm used for detecting the incoming angles.

To determine if $\boldsymbol{p}^t_{\text{RTK}}$ is subjected to a malicious attack, we suggest using one of two detection methods. The first suggestion is based on a Kalman filter and the second is based on position compared to estimated covariance.

C. Kalman filter detection

The first suggested method is a supervisor module which is based on the following state-space model and measurement vector:

$$\dot{\boldsymbol{x}}_1 = \boldsymbol{x}_2 \tag{20}$$

$$\dot{\boldsymbol{x}}_2 = \boldsymbol{w} \tag{21}$$

$$\boldsymbol{z} = \boldsymbol{x}_1 = \hat{\boldsymbol{p}}^t_{tb,\text{PARS}} - \hat{\boldsymbol{p}}^t_{\text{RTK}} \tag{22}$$

used to estimate the difference between position estimates of the INSs with RTK and PARS aiding, respectively. $\boldsymbol{w}$ is some Gaussian process noise. This results in the Kalman filter:

$$\dot{\boldsymbol{x}} = \boldsymbol{F}\boldsymbol{x} + \boldsymbol{K}_s(\boldsymbol{z} - \boldsymbol{H}\boldsymbol{x}), \tag{23}$$

$$\boldsymbol{K}_s = \boldsymbol{P}_s\boldsymbol{H}^\intercal\boldsymbol{R}_s^{-1} \tag{24}$$

$$\dot{\boldsymbol{P}}_s = \boldsymbol{F}\boldsymbol{P}_s + \boldsymbol{P}_s\boldsymbol{F}^\intercal - \boldsymbol{K}_s\boldsymbol{R}_s\boldsymbol{K}_s^\intercal + \boldsymbol{E}\boldsymbol{Q}_s\boldsymbol{E}^\intercal \tag{25}$$

where

$$\boldsymbol{F} = \begin{pmatrix} \boldsymbol{0}_{3x3} & \boldsymbol{I}_3 \\ \boldsymbol{0}_{3x3} & \boldsymbol{0}_{3x3} \end{pmatrix}, \boldsymbol{H} = \begin{pmatrix} \boldsymbol{I}_3 & \boldsymbol{0}_{3x3} \end{pmatrix}, \boldsymbol{E} = \begin{pmatrix} \boldsymbol{0}_{3x3} \\ \boldsymbol{I}_3 \end{pmatrix}. \tag{26}$$

Concerning the tuning of the KF, we define measurement error covariance:

$$\boldsymbol{R}_s := \boldsymbol{P}_{\text{PARS,pos}} + \boldsymbol{P}_{\text{RTK,pos}}, \tag{27}$$

where $\boldsymbol{P}_{\star,\text{pos}}$ indicates the upper left three by three matrix of the full covariance matrix $\boldsymbol{P}_\star$, obtained from the two TMOSs in [6]. $\boldsymbol{Q}_s$ is consider a tuning matrix chosen dependent on how responsive one would like the filter to be. The RTK measurement is considered to be spoofed if the output of the RTK-aided INS differ from that of the INS aided by PARS. The INS position to the user is then given by the module:

$$\hat{\boldsymbol{p}}^t_{\text{robust}} = \begin{cases} \hat{\boldsymbol{p}}^t_{tb,\text{RTK}} & \text{if } ||\boldsymbol{x}_1|| < \theta_{\text{threshold}}(t), \\ \hat{\boldsymbol{p}}^t_{tb,\text{PARS}} & \text{otherwise,} \end{cases} \tag{28}$$

where $\theta_{\text{threshold}}(t)$ is a user-defined threshold. This threshold should typically vary with the distance from the PARS to the UAV as the uncertainty of the PARS position measurements in Cartesian coordinates increases proportionally with the range.

D. Covariance based detection

The second method is based on a twofold strategy:

- Monitoring the discrepancy between the two observer outputs
- Monitoring the residuals of the two observers

The discrepancy between the observer is monitored using

$$T_{\text{RTK,PARS}} = \tilde{\boldsymbol{p}}^\intercal \left(\boldsymbol{P}_{\text{PARS}} + \boldsymbol{P}_{\text{RTK}}\right)^{-1} \tilde{\boldsymbol{p}} \sim \chi^2_3. \tag{29}$$

The observer position difference is given as $\tilde{\boldsymbol{p}} = \hat{\boldsymbol{p}}^t_{tb,\text{PARS}} - \hat{\boldsymbol{p}}^t_{tb,\text{RTK}}$ resulting in $T_{\text{RTK,PARS}}$ being chi-squared distributed, [17]. Combining this with using e.g. a CUSUM [18] algorithm to monitor the mean of the residual in the given observers one can conclude that GNSS is spoofed if

1) The mean of $\tilde{\boldsymbol{y}}^t$ in the RTK aided observer changes
2) The mean of $\tilde{\boldsymbol{y}}^t$ in the PARS aided observer does not change
3) $T_{\text{RTK,PARS}}$ surpasses the critical value of $\chi^2_{\alpha,3}$

where α is the significance value of choice. This results in the default ($\mathcal{H}_0$) and alternative hypothesis ($\mathcal{H}_1$)

$$\begin{aligned} \mathcal{H}_0 &: \quad \boldsymbol{p}^t_{\text{RTK}} \text{ is a valid position measurement.} \\ \mathcal{H}_1 &: \quad \boldsymbol{p}^t_{\text{RTK}} \text{ is subjected to a spoofing attempt.} \end{aligned}$$

E. Output smoothing

To prevent switching back and forth between the two INS's when the difference between the sensors are around the threshold value, hysteresis functionality can be implemented. This can both be done on the detection level, to avoid that spikes in the observer's state estimates too strongly influences the detector, and on the output level to guarantee that the spoofing attack has terminated before switching back. Moreover, since the position, velocity and attitude estimates will be considered by the autopilot, the output of the supervisor can be weighted when switching between the two hypothesis to prevent steps in the INS data. This can be done using exponential function such that

$$\hat{\boldsymbol{p}}^t_{\text{robust}} = \left(1 - \mathrm{e}^{-\alpha(t-t_0)}\right) \hat{\boldsymbol{p}}^t_{tb,\text{PARS}} + \mathrm{e}^{-\alpha(t-t_0)} \hat{\boldsymbol{p}}^t_{tb,\text{RTK}}, \tag{30}$$

when switching between the RTK-based INS and the PARS-based. α is a tuning variable and t_0 is the time of the switch between $\hat{\boldsymbol{p}}^t_{tb,\text{RTK}}$ and $\hat{\boldsymbol{p}}^t_{tb,\text{PARS}}$ as the module output.

V. Experimental Setup

A. Payload

To verify the validity of the observer and supervisor, an experiment was carried out on December 14th 2017 in good, although cold, weather conditions at Agdenes outside of Trondheim, Norway. A flight of 37 min with a Skywalker X8 UAV was performed. The avionics of the UAV consisted of a Pixhawk autopilot [19] with a standard sensor suite and a 3DR GPS module. Along with other sensors, the avionics includes an integrated MEAS MS5611 [20] barometer and a Honeywell HMC5883L digital compass [21], which are both used by the observers. The main telemetry link was the Radionor Communications CRE2 144-LW PARS, depicted in Fig. 6, and a 433 MHz 3DR radio served as a redundant telemetry link.

In addition to the avionics, the SenTiStack was used to achieve a highly accurate navigation solution. The SenTiStack consists of SenTiBoard (previously named SyncBoard [22]) hardware sensor timing board, an Odroid XU4 onboard computer [23], a uBlox M8T GNSS receiver [24], and a tactical grade IMU, which in this experiment was the Sensonor STIM 300 [25]. A schematic overview of the UAV payload and ground station is given in Fig. 7 and a track of the UAV flight is given in Fig. 8.

B. Ground station

To pilot the UAV, register base GNSS data for the RTK solution, and calculate the PARS positioning data, a ground station was set up. This consisted of a laptop computer, a uBlox M8T GNSS receiver, and a Radionor Communications CRE2 189 PARS. The CRE2 189 radio consists of an array of 8×8 antenna elements, and the PARS system was set to operate in a 15 Mbit/s mode, providing a maximal distance of up to 15 km. The ~~PARSs~~PARS modules communicate in the 5 GHz band.

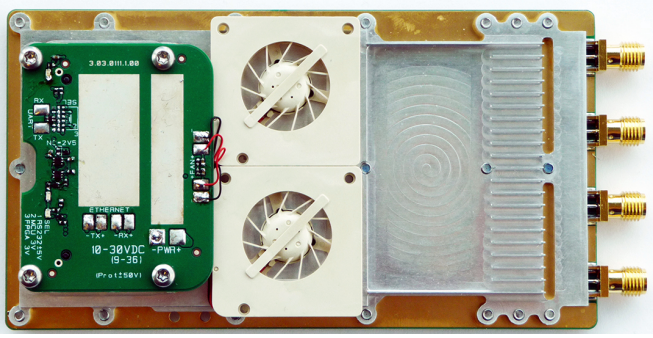

Fig. 6. The Radionor CRE2 144-LW PARS.

C. RTK Spoofing

To simulate a spoofing process of the RTK positioning, we imagine that a malicious agent wants to create an offset to

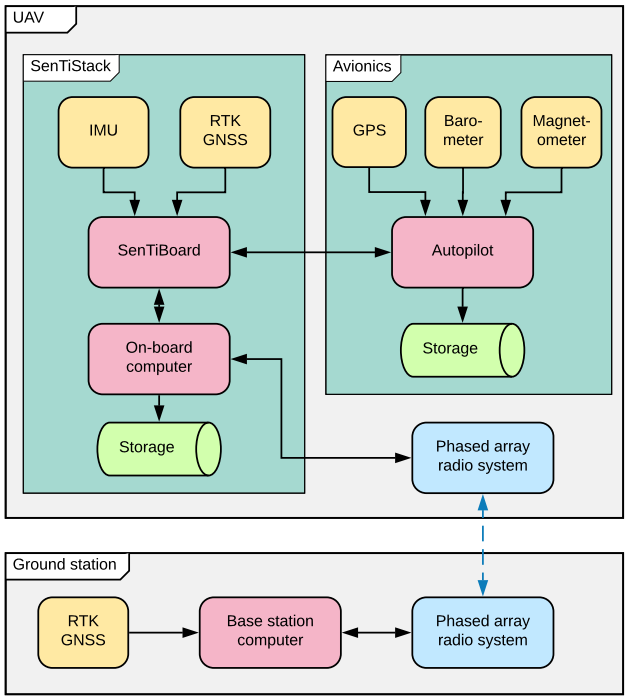

Fig. 7. System overview of the UAV payload and ground station.

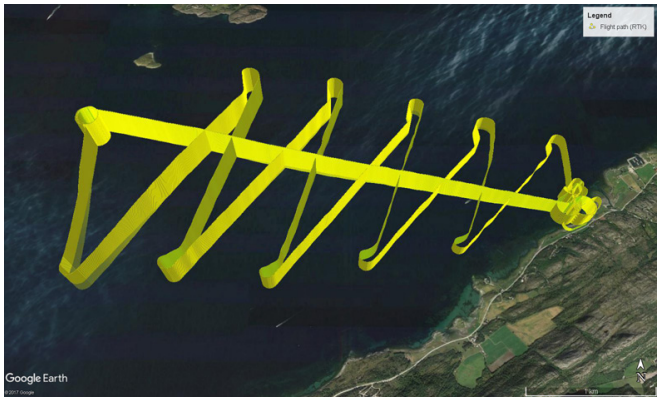

Fig. 8. Track of the UAV flight, based on RTK GNSS position.

the on-board-calculated position of the UAV. If we assume that the intended landing area is close to the take-off area, and the malicious agent observes the take-off of the UAV, the agent can calculate a position offset that would deceive the positioning system into flying the UAV to a different area when it returns for landing. In this scenario the malicious agent can slowly adjust the offset to make it difficult to detect the spoofing process by using inertial sensors.

VI. RESULTS

A. Spoofing setup

In this experiment we set up the RTK-spoofing procedure to initiate 907.6 s after takeoff and create an offset to the RTK-signal, increasing with 0.1 m per sample at a sample rate of 10 Hz, resulting in a velocity change of $1\,\mathrm{m\,s^{-1}}$ until an offset of -1000 m in both East and North direction is reached. Furthermore, we imagine that after the malicious agent discovered that the GNSS-spoofing attempt was ineffective, the spoofing attempt is terminated after being active for 1000 s, at 1907.5 s after take-off. This allows us to show the automatic recovery-feature of the supervisor filter.

Fig. 9 illustrates the observer outputs from the observer using real RTK measurements and the observer using spoofed RTK measurements. It also indicates when the GNSS-spoofing is active. The spike that occurs on the spoofed input at the end of the spoofing period is due to inaccurate velocity estimates which are induced due to the large correction in position when the position measurement snaps back.

B. Tuning

Both the RTK and PARS aided NLOs and TMOs were tuned equivalent with the exception of the $\boldsymbol{R}$ matrices in the TMOs. The $\boldsymbol{Q}$ and $\boldsymbol{R}_\star$ matrices were set as follows:

$$\boldsymbol{Q} = \mathrm{diag}\left(0.0308^2 \cdot \boldsymbol{I}_3, 50 \cdot \boldsymbol{I}_3\right).$$
$$\boldsymbol{R}_{\mathrm{PARS}} = \mathrm{diag}\left(5^2, (2^\circ)^2, 0.5^2\right),$$
$$\boldsymbol{R}_{\mathrm{RTK}} = \mathrm{diag}\left(0.05^2, 0.05^2, 0.1^2\right).$$

The $\boldsymbol{Q}$ matrix of the first version of the supervisor was chosen as $\boldsymbol{Q}_s = \mathrm{diag}\,(1, 1, 0.5)$, and the spoofing-threshold, $\theta_{\mathrm{threshold}}(t)$, was set to the largest value of 20 m and $0.015 \cdot \rho_m$ at the given timestep. Furthermore we added a hysteresis function so that three consecutive position measurements must be classified as inaccurate before the supervisor evaluates that the system is being spoofed and outputs the more robust measurement. For the second method, based on covariance a threshold value of 18^2 m^2 was chosen.

C. Performance metrics

To compare the performance of the different filter setups the following metrics are used: Absolute mean error (AME), standard deviation (STD), and root mean squared (RMS).

The absolute mean error is the sum of the absolute difference between the estimate and the reference value, divided by the number of samples. The standard deviation is the square root of the variance of the set, where the variance is the expected value of the squared deviation from the mean. The root mean squared value is the root of the mean of the squared of each of the points in the data set.

Fig. 10 plots the output of the detector with both RTK measurements and spoofed RTK measurements as references. A line indicating when spoofing is detected is also given. Table I lists the actual starting and ending times of the RTK spoofing, and the offset at the given times. The period when spoofing is detected, and the distance between the RTK and spoofed RTK observers at these times are also given in this table.

In Tables II and III the performance metrics for the RTK observer and the PARS observer when they are compared to the RTK measurements are listed. An error-plot of the detector output compared to the RTK measurements is given in Fig. 11.

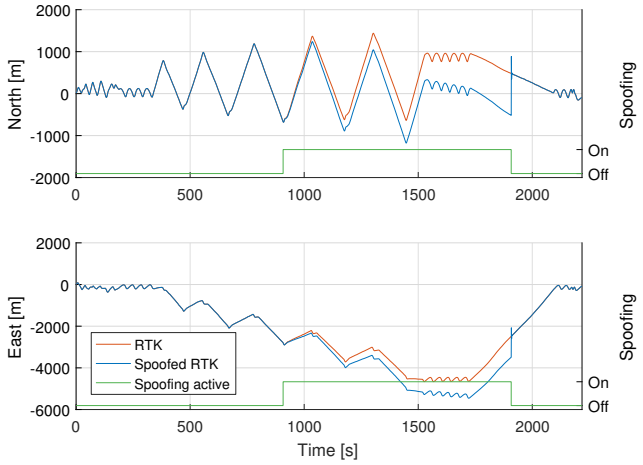

Fig. 9. RTK filter output with and without spoofing. The green line indicates when the spoofing is active.

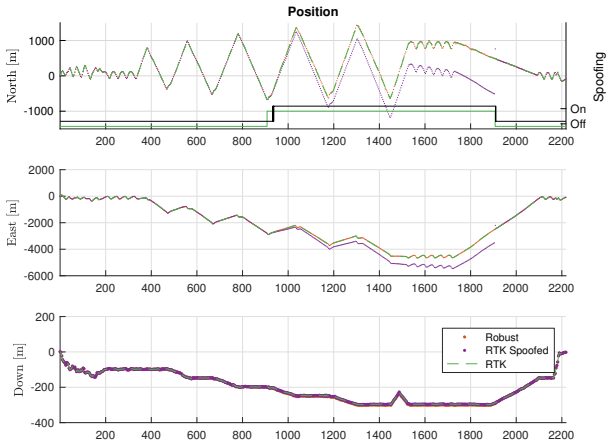

Fig. 10. Output of the detector plotted against spoofed filter output. The dashed green line is the un-spoofed RTK solution provided as a reference. The black 'spoofing' line shows when the filter detects a spoofing attempt, while the solid green line shows when the spoofing is active.

D. Discussion

From the results provided in this section we see that when the spoofing attack is recognized by the detector as intended as the magnitude of the spoofed offset becomes significant. Furthermore we see that the system output of the detector changes according to the estimated spoofed state, and that it recovers as intended. The computational overhead of using these detection methods is primarily due to running the two observers in parallel, as the supervisor module is lightweight.

As illustrated in Fig. 12, the spoofing observer also handles a spoofing attack with a slower change in position. We can see that the time before the attack can be detected by the filter increases, which is expected as the impact of the attack is less severe. However, as the offset increases, this spoofing is also detected. The time before asserting a detection can be reduced by lowering the threshold value, but this will increase the likelihood of false positives.

TABLE I

DETECTOR KEY-FIGURES. TIME MEASUREMENTS ARE GIVEN AS SECONDS AFTER TAKE-OFF AND DISTANCE MEASUREMENTS ARE GIVEN AS THE 2-NORM OF THE DIFFERENCE FROM THE OUTPUT FROM THE OBSERVER WITH THE NON-SPOOFED RTK POSITION REFERENCE.

	Start [s]	**End [s]**	**Offset [m]**	**End offset [m]**
Actual:	907.60	1907.50	0.00	1414.35
Detector:	932.89	1910.89	35.97	22.98

TABLE II

PARS OBSERVER PERFORMANCE COMPARED TO RTK MEASUREMENTS, IN METERS

	North	**East**	**Down**	**Norm**
AME:	7.76	4.48	3.18	9.51
STD:	10.35	3.55	0.78	10.97
RMS:	11.00	5.31	3.28	12.65

Although the results in this paper looks promising, more testing should be done before concluding on the reliability of the PARS as a position sensor. The occurrence of an errors, possibly due to reflections of the PARS signal, may be more likely than a spoofing attack, especially in short intervals where the PARS measurements are inaccurate.

VII. CONCLUDING REMARKS

In this paper we have implemented a drift-free positioning system that automatically detects and handles spoofing of GNSS positioning solutions. By using a phased array radio system (PARS), which is robust against malicious attacks such as spoofing and jamming, as a secondary position reference, we are able to maintain security of the UAV even during spoofing attacks on the UAV.

An experiment was carried out and a simulated spoofing attempt was added in software. With our defined threshold the spoofing attempt was first detected when the RTK estimate was approximately 36 m away from the expected value. Furthermore we showed that the supervisor automatically recovered to the high-quality position estimate when the spoofing attempt was terminated.

A. Future work

To improve the position estimates from the radio observer, we would like to implement a tightly coupled observer for the PARS. We would also like to compare our current method with one that compensates for the curvature of the Earth.

To be able to use the PARS as a spoofing detector in a real-life scenario, further testing and robustification of

TABLE III

RTK OBSERVER PERFORMANCE COMPARED TO RTK MEASUREMENTS, IN METERS

	North	**East**	**Down**	**Norm**
AME:	0.02	0.02	0.03	0.04
STD:	0.03	0.02	0.04	0.06
RMS:	0.03	0.02	0.05	0.06

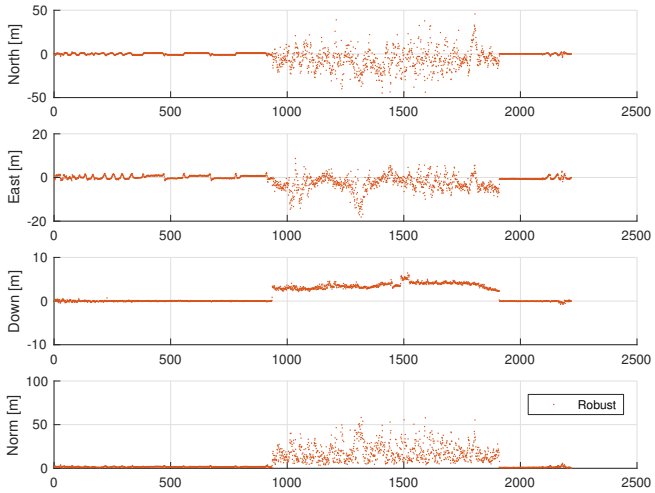

Fig. 11. Error of the detector output compared to RTK measurements.

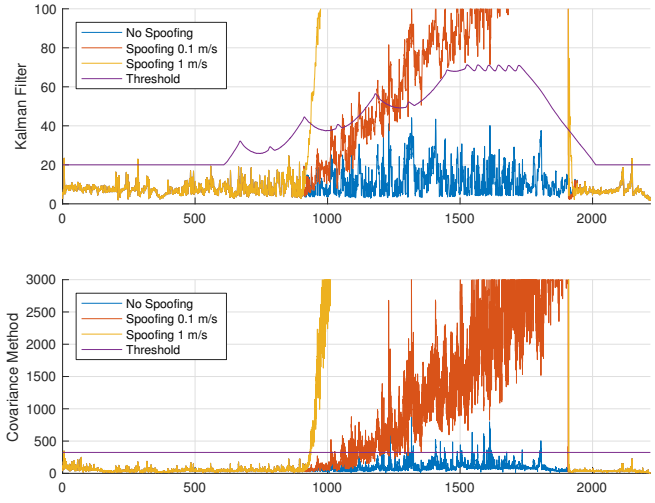

Fig. 12. Detector calculations and threshold. A spoofing attack with an offset-velocity of $0.1\,\mathrm{m\,s^{-1}}$ is added to show the difference in behaviour.

the direction-of-arrival detection should be performed. In addition we would like to extend the observer to support measurements from multiple ground radios simultaneously. We would also like to implement a system that automatically detects hand-overs from one ground radio to another when flying in-between visible sectors.

Finally, we would like to be able to compensate for reflections in the ocean surface. By altering the algorithm that calculates the bearing and elevation from the incoming radio signals, we could obtain several possibilities for each frame, and employ methods like multiple hypothesis tracking to better estimate these measurements.

ACKNOWLEDGMENT

The authors thank Atle Sægrov and Tor Berg at Radionor Communications for allowing us to use the PARS equipment their support with the PARS positioning system. Furthermore we thank our skillful pilots, Lars Semb and Pål Kvaløy, for their assistance both at the lab and in the field.

REFERENCES

[1] A. Pinker and C. Smith, "Vulnerability of the GPS signal to jamming," *GPS Solutions*, vol. 3, no. 2, pp. 19–27, 1999.
[2] A. J. Kerns, D. P. Shepard, J. A. Bhatti, and T. E. Humphreys, "Unmanned aircraft capture and control via GPS spoofing," *Journal of Field Robotics*, vol. 31, no. 4, pp. 617–636, 2014.
[3] B. Starr and R. Browne, "Ash Carter: 'Navigational error' behind U.S. sailors ending up in iran," CNN: http://edition.cnn.com/2016/01/14/politics/navy-boats-iran-waters/index.html, January 15 2016.
[4] A. Jafarnia-Jahromi, S. Daneshmand, and G. Lachapelle, "Spoofing countermeasure for GNSS receivers–a review of current and future research trends," *Proc. on the 4th Intern Colloquim on Scientific and Fundamental Aspects of the Galileo Programme*, pp. 1–8, 2013.
[5] S. M. Albrektsen, A. Sœgrov, and T. A. Johansen, "Navigation of UAV using phased array radio," in *Workshop on Research, Education and Development of Unmanned Aerial Systems (RED UAS)*, 2017.
[6] S. M. Albrektsen, T. H. Bryne, and T. A. Johansen, "Phased array radio system aided inertial navigation for unmanned aerial vehicles," in *Proc. of the IEEE Aerospace Conference*, Big Sky, Montana, March 3–10 2018.
[7] M. L. Psiaki, T. E. Humphreys, and B. Stauffer, "Attackers can spoof navigation signals without our knowledge. Here's how to fight back GPS lies," *IEEE Spectrum*, vol. 53, no. 8, pp. 26–53, 2016.
[8] J. A. Farrell, *Aided Navigation: GPS with High Rate Sensors*. McGraw-Hill, 2008.
[9] H. Krim and M. Viberg, "Two decades of array signal processing research: the parametric approach," *IEEE Signal Processing Magazine*, vol. 13, no. 4, pp. 67–94, Jul 1996.
[10] R. Schmidt, "Multiple emitter location and signal parameter estimation," *IEEE Transactions on Antennas and Propagation*, vol. 34, no. 3, pp. 276–280, Mar 1986.
[11] R. Roy and T. Kailath, "ESPRIT-estimation of signal parameters via rotational invariance techniques," *IEEE Transactions on Acoustics, Speech, and Signal Processing*, vol. 37, no. 7, pp. 984–995, Jul 1989.
[12] D. H. Titterton and J. L. Weston, *Strapdown inertial navigation technology*, 2nd ed. Institution of Electrical Engineers and American Institute of Aeronautics and Astronautics, 2004.
[13] Y. Bar-Shalom and X.-R. Li, *Multitarget-Multisensor Tracking: Principles and Techniques*. YBS Publishing, 1995.
[14] H. F. Grip, T. I. Fossen, T. A. Johansen, and A. Saberi, "Nonlinear observer for GNSS-aided inertial navigation with quaternion-based attitude estimation," in *Proc. of the American Contr. Conf.*, Washington, DC, June 2013, pp. 272–279.
[15] M. G. Petovello, K. O'Keefe, G. Lachapelle, and M. E. Cannon, "Consideration of time-correlated errors in a Kalman filter applicable to gnss," *Journal of Geodesy*, vol. 83, no. 1, pp. 51—56, 2009.
[16] T. H. Bryne, J. M. Hansen, R. H. Rogne, N. Sokolova, T. I. Fossen, and T. A. Johansen, "Nonlinear observers for integrated INS/GNSS navigation – Implementation aspects," *IEEE Control Systems Magazine*, vol. 37, no. 3, pp. 59–86, 2017.
[17] F. Gustafsson, *Statistical Sensor Fusion*, 2nd ed. Studentlitteratur AB, 2012.
[18] E. S. Page, "Continuous inspection schemes," *Biometrika*, vol. 41, no. 1-2, pp. 100–115, 1954.
[19] L. Meier, D. Honegger, and M. Pollefeys, "PX4: A node-based multithreaded open source robotics framework for deeply embedded platforms," in *IEEE International Conference on Robotics and Automation (ICRA)*, May 2015.
[20] *MS5611-01BA03 Barometric Pressure Sensor*, Measurement Specialties, 9 2015.
[21] *3-Axis Digital Compass IC HMC5883L*, Honeywell, 2 2013, rev. E.
[22] S. M. Albrektsen and T. A. Johansen, "SyncBoard - a high accuracy sensor timing board for UAV payloads," in *International Conference on Unmanned Aircraft Systems (ICUAS)*, June 2017, pp. 1706–1715.
[23] *User Manual ODROID-XU4*, Hard Kernel, 2015.
[24] *u-blox 8 / u-blox M8 Receiver Description*, u-blox, May 2016, r11.
[25] *STIM300 Inertia Measurement Unit*, sensonor, Apr. 2013, rev. 8.